Electronic and Nuclear Dynamics of the Accessory Bacteriochlorophylls in Bacterial Photosynthetic Reaction Centers from Resonance Raman Intensities

Nerine J. Cherepy,[†] Andrew P. Shreve,[†,§] Laura J. Moore,[‡] Steven G. Boxer,[*,‡] and Richard A. Mathies[*,†]

Department of Chemistry, University of California, Berkeley, California 94720, and Department of Chemistry, Stanford University, Stanford, California 94305

Received: October 3, 1996; In Final Form: January 8, 1997[⊗]

Resonance Raman spectra and absolute Raman scattering intensities of the Franck−Condon coupled vibrational modes of the accessory bacteriochlorophylls (B) in the photosynthetic reaction center from *Rb. sphaeroides* have been obtained with excitation in their 800 nm Q_y absorption band. Although the relative Raman intensities are unchanged when the temperature is reduced from 278 to 95 K, the absolute Raman scattering intensity is found to increase by a factor of ∼4 at 95 K. A self-consistent multimode vibronic model for the excited-state properties of B has been developed that provides a unique fit to the absorption band and the Raman cross sections at both temperatures using a total *S* (linear electron−nuclear coupling factor) of 0.32 and an effective electronic dephasing time of ∼54 fs at 278 K and ∼210 fs at 95 K. The Raman scattering cross sections are consistent with an electronic structure model where the two B chromophores absorb and scatter independently. The Raman cross sections scale as $1/T^2$ in the 95−298 K range, suggesting that the pure dephasing time, if modeled as a Gaussian (slow-modulation limit), decreases linearly with temperature. At room temperature, the electronic dephasing time is controlled by bath-induced dephasing processes rather than the energy transfer time from the excited state of B. The electronic and nuclear relaxation parameters derived here provide a more quantitative picture of the time scale and structural relaxation of the chromophores involved in energy transfer in reaction centers.

Introduction

The photosynthetic reaction center (RC)[1] is a pigment-protein complex in which a highly efficient light-driven electron transfer reaction occurs.[2−6] The bacterial reaction center of *Rhodobacter sphaeroides* has an approximate C_2 axis of symmetry around which lie a bacteriochlorophyll (BChl) dimer called P, two monomeric BChls called B_A and B_B, and two bacteriopheophytin (BPheo) molecules called H_A and H_B. The lowest energy, near-infrared absorption bands of *Rb. sphaeroides* RCs result from the Q_y electronic transitions of P, B, and H which in the room-temperature spectrum are near 870, 800, and 760 nm (Figure 1). The 870 nm absorption is due to the lower exciton band of P, the 800 nm band is due to the overlapping absorptions of B_A and B_B, and the 760 nm band is due to H. Charge separation between the special pair and one of the bacteriopheophytin molecules (H_A) is complete within about 3 ps at room temperature,[7−12] and in about half that time at 100 K.[13] The role of the accessory bacteriochlorophyll B_A in the RC is enigmatic; upon excitation both B_A and B_B transfer energy to P within ∼100 fs,[8,14,15] while B_A may also be involved in the electron transfer from the excited state of P to H_A. The role of B_A in mediating charge separation is still unresolved.[16−18]

We are interested in elucidating the electronic and nuclear properties of B. The conformation, electronic structure and the extent of electron−nuclear coupling of B appear to be relatively unperturbed from that of BChl itself. For example, the Raman spectrum of B as well as Stark effect spectra are very similar to spectra obtained from BChl in solution or films.[19−23] No quantitative measurements of the electron−nuclear coupling in the Q_y band of B have been made; however, other protein-bound monomeric Chls and BChls exhibit weak coupling, characterized by a total linear electron−nuclear coupling constant (the Huang−Rhys factor or *S*) of ∼0.5.[24,25] The extent of excitonic coupling between B and the other RC chromophores must also be known to define the character of the optically pumped states. Finally, the determination of the excited-state dephasing time of B and its temperature dependence would provide information about the pure dephasing processes coupled to B.

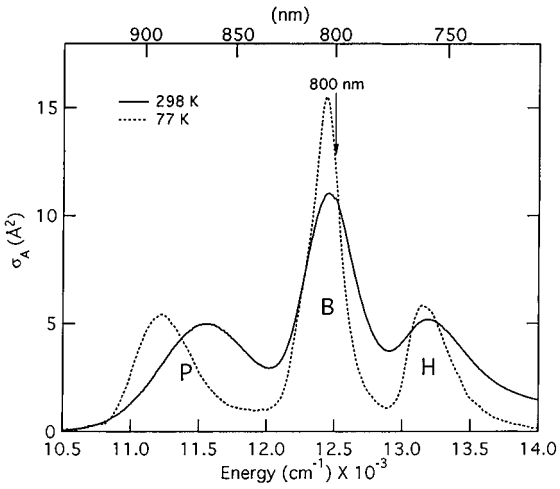

Figure 1. Near-IR absorption spectrum of R-26 *Rb. sphaeroides* reaction centers at 298 and 77 K (10 mM TRIS, 1 M EDTA, 0.1% LDAO, 50% glycerol). The 800 nm excitation wavelength used to acquire Raman spectra is indicated by the arrow.

Resonance Raman vibrational spectroscopy and Raman intensity analysis are powerful methods for obtaining information about the multimode nuclear and electronic dynamics of

[†] University of California at Berkeley.
[‡] Stanford University.
[§] Current address: Los Alamos National Laboratory, CST-4, MS G755, Los Alamos, NM 87545.
* To whom correspondence should be addressed.
[⊗] Abstract published in *Advance ACS Abstracts,* March 15, 1997.

S1089-5647(96)03051-9 CCC: $14.00

excited states.[26−30] The modes that appear in a resonance Raman spectrum are those that couple to the resonant electronic transition, and the intensity of the Raman scattering reflects both the strength of this coupling and the dynamics that occur in the excited electronic state. A self-consistent model of the absorption spectrum and the excitation-wavelength-dependent resonance Raman cross sections can be used to develop a multidimensional excited-state potential energy surface model and a description of the electronic state relaxation rates, as has been demonstrated for other photobiological systems.[28,31,32] Furthermore, the temperature dependence of Raman intensities is useful to further delimit the strength of mode coupling and to assign broadening mechanisms.

Here we present a quantitative analysis of the electronic and nuclear dynamics of B, based on an analysis of its Raman and absorption spectra. This includes (i) acquiring a complete set of Raman spectra taken with 800 nm Q_y excitation at both 95 and 278 K, (ii) quantifying the scattering strength at several excitation wavelengths resonant with the B absorption band and at several temperatures by using an internal scattering standard, and (iii) using these data to perform self-consistent multimode vibronic modeling of the absorption spectrum and Raman excitation profiles. We found previously that the absolute intensity of the Raman scattering for the 731 cm^{-1} mode of B is about an order of magnitude larger than that of P at 278 K.[33] Here we extend this observation by showing that the Raman cross section of the 731 cm^{-1} B mode increases by an additional factor of ∼4 when the temperature is decreased from 278 to 95 K. The model of the photophysics of B developed here is valuable because it defines the multimode electron−nuclear coupling constants and the temperature dependent dephasing rates of a key component of the reaction center.

Experimental Section

RCs were isolated from the R-26 mutant of *Rb. sphaeroides* as described previously.[34,35] For the experiments at 278 K, Q_A-containing RCs were suspended in buffered detergent solution (0.025% LDAO, 10 mM TRIS, pH 8) or in a solution of buffered detergent and 50% ethylene glycol. Measurements of the Raman intensities at 278 K were also carried out on a 50% ethylene glycol sample in which P is oxidized with 40 mM $K_3Fe(CN)_6$. To produce optically clear glasses at 95 K, solutions of RCs in buffered detergent and 60% glycerol were used. For the low-temperature intensity measurements, the RCs were suspended in a buffered solution containing 30% glycerol and 50% ethylene glycol.

The laser excitation and collection of scattered light from a rapidly flowing solution of RCs at 278 K were performed as described previously.[33,36] Excitation powers at all temperatures were typically 5 mW for measuring the full spectrum, and 2 mW for measuring the relative intensities in the 50% ethylene glycol solution. The low-temperature experiments employed a Harney−Miller cell in which the sample, held in a 1 mm i.d. capillary, is cooled by circulating cold N_2 gas through the cell; the temperature was monitored with an iron−constantin thermocouple next to the capillary. Raman spectra were recorded with a cryogenically cooled CCD detector (LN/CCD-1152, Princeton Instruments) coupled to a subtractive-dispersion, double spectrograph[37] equipped with one 600 g/mm grating and one 1200 g/mm grating, both blazed at 750 nm (10 cm^{-1} entrance slit). All spectra were corrected for the wavelength dependence of the system by use of a standard lamp.

We have employed the shifted-excitation Raman difference spectroscopy (SERDS) technique described in our earlier work,[33,36,38−40] to acquire Raman spectra in the presence of a substantial fluorescence background due to intrinsic fluorescence and to very small concentrations of impurities. The accuracy of this method has been demonstrated by comparing directly detected spectra with the SERDS regenerated Gaussian spectra (see below and refs 36 and 38).

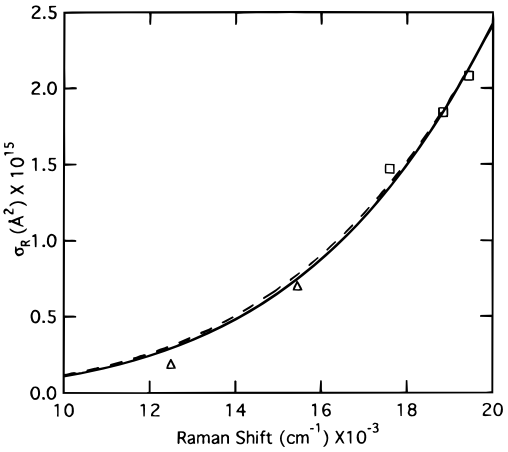

Figure 2. Raman scattering cross section for the 864 cm^{-1} mode of ethylene glycol as a function of excitation wavelength. The squares were measured previously in our laboratory.[41] The open triangles are the results of measurements reported here. The dashed line is a fit to the previous data only using eq 1 with $\omega_e = 120\,000$ cm^{-1} and $K = 3.03 \times 10^{-10}$ Å^2, while the solid line is a best fit to all five data points using eq 1 with $\omega_e = 95\,565$ cm^{-1} and $K = 1.11 \times 10^{-10}$ Å^2.

Determination of Absolute Raman Cross Sections. Ethylene glycol was used as an internal resonance Raman intensity standard. Raman scattering from the 864 cm^{-1} mode of ethylene glycol can be observed when the RC concentration is reduced enough to compensate for the resonance enhancement of the RC scattering. For quantitative work, the intensity of the strong 731 cm^{-1} RC mode was measured relative to that of the 864 cm^{-1} ethylene glycol mode using a low concentration solution of RCs. Samples for the 278 K experiments had an 800 nm OD of ∼0.15 and samples for the 95 K experiments had an 800 nm OD of ∼0.03.

The absolute cross sections for the 864 cm^{-1} ethylene glycol mode have been previously measured for three excitation wavelengths in the visible.[41] These values were fit using a nonlinear least-squares algorithm to an *A*-term expression in the off-resonance limit:[42,43]

$$\sigma_R(\omega,\omega_s) = K[\omega_s{}^3\omega(\omega_\epsilon{}^2 + \omega^2)^2/(\omega_\epsilon{}^2 - \omega^2)^4] \qquad (1)$$

where ω is the incident frequency, ω_s is the scattered frequency, K is a constant, and ω_e is the effective resonance frequency for the electronic state from which the scattering is derived. The three visible excitation wavelengths used in the work of Lawless and Mathies were fit to eq 1 and the extrapolation of that fit to the near infrared is presented in Figure 2.[44]

Because of the long extrapolation required, we measured the ethylene glycol cross sections at 647.1 and 800 nm using the integrating sphere method.[43] To check the reliability of the results, measurements were also performed on cyclohexane and benzene at 647.1 nm where these cross sections have been previously measured and at 800 nm. In general the values we measured for cyclohexane and benzene were systematically ∼10−30% lower than the measured or extrapolated values obtained from previous work in this lab. This discrepancy lies just outside the estimated uncertainties in the measurements but is well within the variation of absolute cross sections reported from different labs (which range up to a factor of 2) when using red excitation wavelengths. The cross sections for ethylene

glycol were 0.7×10^{-15} Å^2 at 647.1 nm and 0.19×10^{-15} Å^2 at 800 nm. These new data and the fit to all five data points with $K = 1.11 \times 10^{-10}$ Å^2 and $\omega_e = 95\,565$ cm^{-1} are shown in Figure 2 (solid line).

It was assumed that the 864 cm^{-1} Raman scattering cross section of ethylene glycol was temperature independent. Our justification for this assumption is based on the observed lack of temperature dependence of the intensity of the ethylene glycol Raman scattering under the same excitation conditions between 278 and 95 K. The preresonant Raman cross sections of propylene glycol were similarly found to be temperature independent between 10 and 290 K by Schomacker and Champion.[32] To calculate the σ_{RC}, the absolute Raman cross section for the 731 cm^{-1} mode of the RC, the following formula for referencing to σ_{EG}, the Raman cross section of the 864 cm^{-1} mode of ethylene glycol, was used:

$$\sigma_{RC} = \frac{I_{RC}}{I_{EG}} \frac{c_{EG}}{c_{RC}} \frac{[(1+2\rho)/(1+\rho)]_{RC}}{[(1+2\rho)/(1+\rho)]_{EG}} \sigma_{EG} \qquad (2)$$

where I is the measured Raman peak area, c is the concentration, ρ is the Raman depolarization ratio, and σ is the Raman cross section. The concentration of RCs was determined through the use of the measured OD and the known extinction coefficient at 802 nm (288 000 M^{-1} cm^{-1}).[45] The depolarization ratio for the 731 cm^{-1} B mode with 800 nm excitation was measured to be 0.30 ± 0.06 and that for the 864 cm^{-1} mode of ethylene glycol with 800 nm excitation was 0.16 ± 0.03. The depolarization ratios for the other B modes range from 0.29 to 0.51, but for our analysis we have calculated the relative intensities of all modes relative to the 731 cm^{-1} mode. This simplification will not greatly impact our analysis, as the correction would be rather minor (<10%).

Theoretical Modeling. A thermally averaged time-correlator formulation, previously described in detail by Shreve and Mathies,[46] was used to calculate the Raman scattering and the absorption cross sections in the Condon limit. The parameters for a self-consistent model consist of the homogeneous and inhomogeneous line width for the electronic transition and the linear electron−nuclear coupling constants or S's for all the modes (where $S = \Delta^2/2$ and Δ is the dimensionless displacement along each mode). The modeling protocol assumed that the ground-to-excited state displacements and the transition moment were temperature independent, while the inhomogeneous broadening was allowed to remain constant or to decrease with temperature. The reduced 17-mode model is detailed in Table 1.[47] The absorption band fitting at 278 K utilized an absorption spectrum from which an estimate of the asymmetric Gaussian lower exciton band of P was subtracted. This estimate was generated from a vibronic model of the P band that will be reported separately.[48] We also assume that the two B molecules are coupled to comparable modes with the same electron−nuclear coupling constants. This is justified by the lack of Raman spectral changes as excitation is tuned through the B band.

Results

The resonance Raman spectra of B excited at 800 nm at 278 and 95 K are presented in Figure 3A,B, respectively. The raw data, the least-squares fits to these data, the residuals, and the regenerated spectra are presented in each case. At 95 K, the Raman cross sections for B are large enough relative to the background fluorescence that a flat-field corrected spectrum can also be taken. Figure 3B compares the SERDS difference spectrum with the flat-field corrected spectrum. The excellent agreement for both the peak positions and amplitudes between the spectrum regenerated from the fit to the SERDS spectrum and the directly detected spectrum provides a clear demonstration of the accuracy and validity of the SERDS-acquired data.

The vibrational frequencies and relative intensities at 95 and 278 K are compared in Table 1. Table 1 also shows how the modes are grouped for the 17-mode model. All the Raman lines reported previously[33,36] in the B spectrum at 278 K are observed,

TABLE 1: Frequencies and Intensities of B Raman Bands

B at 95 K		B at 278 K		17-mode model		
ω, cm^{-1}	intensity[a]	ω, cm^{-1}	intensity[b]	ω, cm^{-1}	intensity (95 K)	intensity (278 K)
84	0.55	*c*		84	0.55	0.55
121	0.47	117	0.35	117	0.47	0.35
160	0.10			177	1.12	1.43
186	1.02	177	1.43			
219	0.56	212	1.30	212	0.56	1.30
334	0.40	332	0.63	332	0.40	0.63
358	0.73	355	0.49	355	0.73	0.49
383	0.58	384	0.51	384	0.89	0.59
398	0.31	397	0.08			
417	0.30	418	0.05			
436	0.14	436	0.03			
464	0.03	464	0.05	464	0.53	0.20
479	0.04	478	0.06			
511	0.02	512	0.01			
568	0.55	569	0.41	569	0.55	0.41
624	0.19	621	0.16			
685	0.40	682	0.28	682	0.59	0.47
726	0.23	721	0.12			
736	0.57	731	0.78	731	1.00	1.00
747	0.20	744	0.10			
765	0.19	761	0.18	761	0.19	0.18
843	0.17	843	0.13			
894	0.82	892	0.67	892	0.99	0.80
921	0.06	920	0.09			
945	0.06	947	0.04			
967	0.21	970	0.05	1002	1.04	0.55
1000	0.37	1002	0.17			
1021	0.34	1018	0.20			
1065	0.03	1064	0.11			
1082	0.01					
1101	0.03					
1116	0.18	1114	0.14	1114	0.49	0.41
1133	0.24	1132	0.16			
1163	0.44	1158	0.16			
		1165	0.58	1165	0.91	0.9
1185	0.06					
1229	0.10					
1242	0.04					
1269	0.10	*c*				
1280	0.04					
1302	0.02					
1336	0.08					
1346	0.03					
1369	0.05					
1382	0.04					
1393	0.07					
1465	0.01					
1516	0.04					
1534	0.08	*c*		1535	0.39	0.40
1579	0.02					
1652	0.06					
1673	0.02					

[a] Measured Raman intensities at $\lambda_{ex} = 800$ nm are relative to the sum of the intensities of the 726, 736, and 747 cm^{-1} modes from the spectrum in Figure 3A. [b] Measured Raman intensities at $\lambda_{ex} = 800$ nm are relative to the sum of the intensities of the 721, 731, and 744 cm^{-1} modes from the spectrum in Figure 3B. [c] It cannot be determined from the spectra in Figure 3A whether modes are present below 100 cm^{-1} or above 1165 cm^{-1}, so it is assumed that the intensities for the 278 K spectrum match the relative intensities for the 95 K spectrum in these regions.

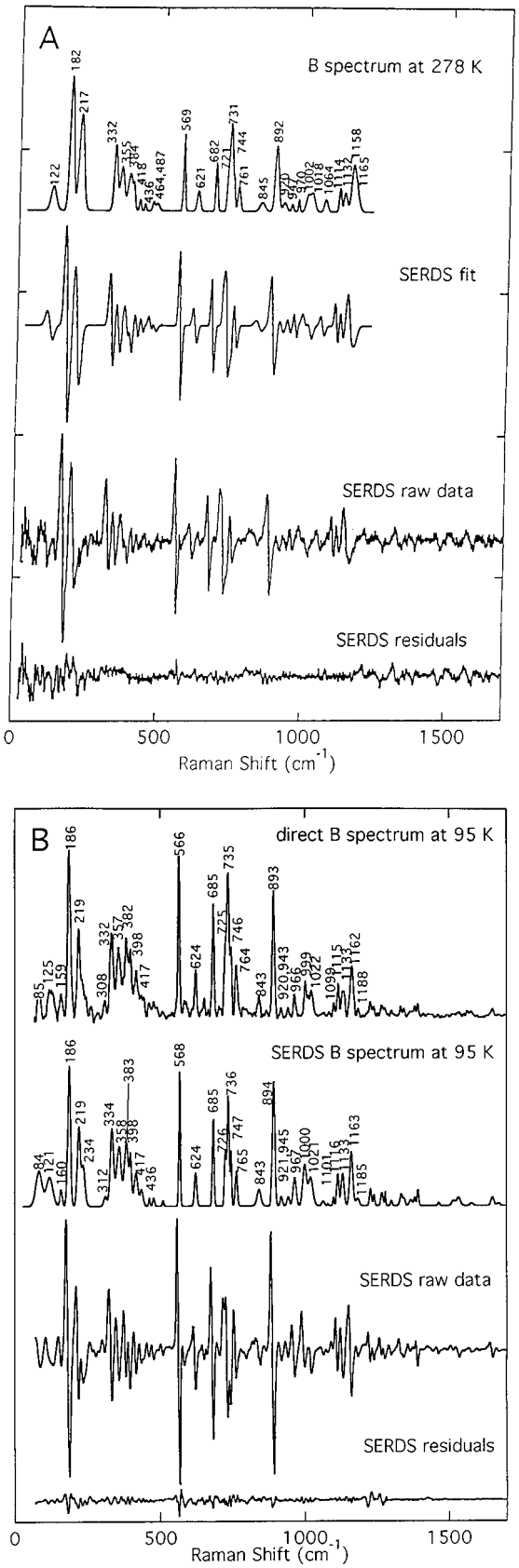

Figure 3. (A) Complete Raman spectrum of B in R-26 RCs obtained using 800 nm excitation at 278 K (power = 5−8 mW). The regenerated spectrum, the least-squares fits to the SERDS data, the raw SERDS data, and the residuals are shown from top to bottom, respectively. (B) Complete Raman spectrum of B obtained using 800 nm excitation at 95 K (power = 5−8 mW). The direct spectrum, the spectrum generated from the least-squares fit to the SERDS data, the raw SERDS data, and the residuals are shown from top to bottom, respectively. The spectra were obtained at both temperatures using a sample having an OD ~3.0/cm (measured at 800 nm and 298 K).

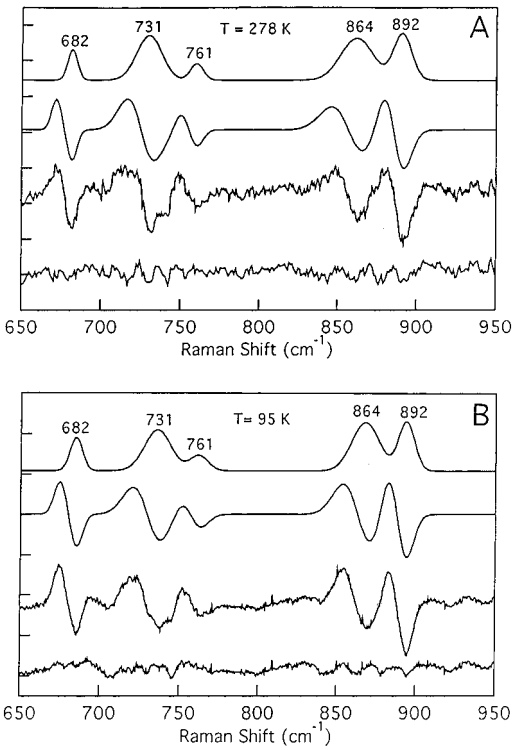

Figure 4. (A) Midfrequency 800-nm excited SERDS Raman spectrum of B at 278 K in a 50% v/v mixture of buffer and ethylene glycol (OD at 800 nm, 298 K = 0.22). The mode at 864 cm^{-1} is the ethylene glycol standard. (B) Midfrequency 800-nm excited SERDS Raman spectrum of B at 95 K in a 50% v/v mixture of buffer and ethylene glycol (OD at 800 nm, 298 K = 0.032).

along with some smaller features which could be observed due to the improved signal-to-noise at 397, 418, 436, 464, 478, 512, 721, 744, 920, 947, 970, 1002, 1064, and 1158 cm^{-1}. Features observed at 1230, 1340, 1352, 1480, 1535, 1590, and 1632 cm^{-1} can be fit but are not much larger than the noise level. The frequencies and relative *intensities* change very little between the two temperatures; the 95 K spectrum contains nearly all the modes seen in the 278 K spectrum along with some new weak modes at 843, 1082, 1101, 1185, 1242, 1269, 1280, 1302, 1369, 1382, 1393, 1516, 1652, and 1673 cm^{-1}. These high-frequency modes can be fit in the low-temperature data due to stronger overall cross sections and higher signal-to-noise.

In separate experiments (not shown) we found that the oxidation of P with $K_3Fe(CN)_6$ does not affect the 278 K Raman intensities of B excited at 800 nm. This demonstrates that the excited-state dephasing time of B which determines the intensity of the Raman cross sections is *not* affected by disruption of the population relaxation pathway, suggesting that an alternate relaxation route, occurs at about the same rate as energy transfer from the excited state of B to P. In agreement with this result, Jia et al. directly measured the population dynamics of B using ultrafast pump−probe techniques, and found that the kinetic component corresponding to energy transfer from B did not change when P was oxidized.[14] Measured Raman intensities of B at 95 and 278 K were independent of the oxidation state of P and were the same for Q_A-containing or Q_A-depleted RCs.

Temperature Dependence. The comparison of the intensities of the 731 cm^{-1} RC mode and the 864 cm^{-1} ethylene glycol standard mode at 278 and 95 K is presented in Figure 4. In the 731 cm^{-1} region in Figure 3A there are three close-lying overlapping modes at 721, 731, and 744 cm^{-1}, and the fits to determine the Raman intensity of the ~731 cm^{-1} mode are really a fit to the broad feature comprising these three modes.

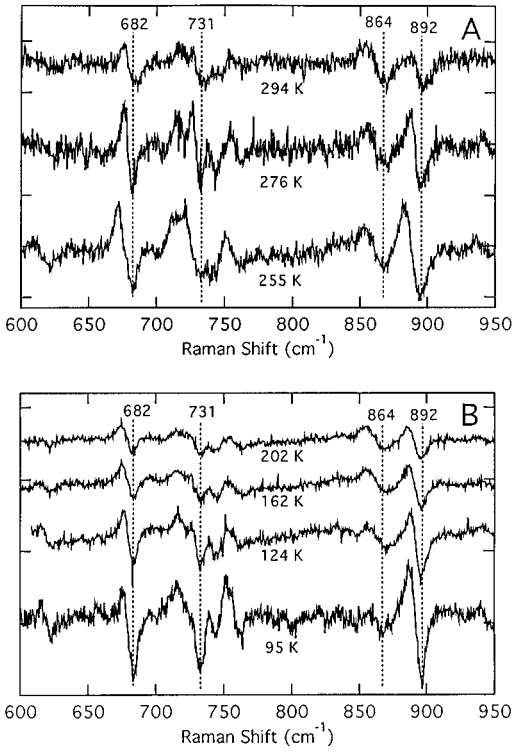

Figure 5. (A) SERDS spectra of B in a 50% v/v mixture of buffer and ethylene glycol at 294, 276, and 255 K (OD at 800 nm, 298 K = 0.25, power at 800 nm = 6 mW). The mode at 864 cm^{-1} is the ethylene glycol standard. (B) SERDS spectra of B in a 50% v/v mixture of buffer and ethylene glycol at 202, 162, 124, and 95 K (OD at 800 nm, 298 K = 0.14, power at 800 nm = 6 mW).

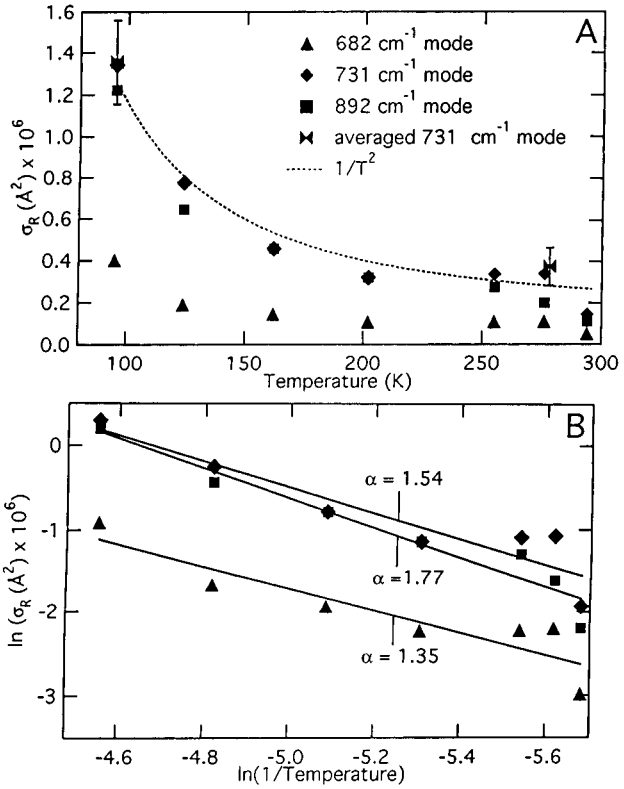

Figure 6. (A) Absolute Raman cross sections as a function of temperature for the 682, 731, and 892 cm^{-1} modes calculated from the data in Figure 5. The uncertainty in the cross sections is ≤30%, based on the uncertainty of the measurements at 95 and 278 K. The measurements at 95 and 278 K for the 731 cm^{-1} mode cross section are also shown along with a plot of $1/T^2$. (B) Plot of $\ln(\sigma_R)$ vs $\ln(1/T)$. The slopes of the best fit lines to the data for the 682, 731, and 892 cm^{-1} modes range from 1.35 to 1.8.

The modeling reflects this by grouping these modes into a single mode at 731 cm^{-1}. The striking feature apparent in Figure 4 is that the RC Raman scattering is of approximately equal intensity at 278 K for a solution which is ~7 times more concentrated than that used at 95 K. The Raman cross section of the 731 cm^{-1} mode with 800 nm excitation at 278 K is (3.7 ± 0.9) × 10^{-7} Å^2 (from six measurements), increasing to (13.6 ± 2.0) × 10^{-7} Å^2 at 95 K (from four measurements).

Several factors contribute to the temperature dependence of the Raman cross sections. First, the absorption coefficient at 800 nm increases by a factor of 1.3 when the temperature is reduced from 298 to 77 K, due to the narrowing of the spectral distribution at low temperature (see Figure 1). Since the Raman cross section scales as M^4 (where M is the transition moment), an increase in Raman cross sections by at least a factor of 1.7 is expected from this effect alone. Our measured increase between 278 and 95 K is ~3.7. The remaining increase in the Raman scattering intensity must be due to reduced dephasing contributions that will be examined in detail below.

Raman spectra acquired on a single sample as a function of temperature are presented in Figure 5. A less concentrated sample was required for the spectra in Figure 5B to maintain an easily measurable intensity ratio between the RC and the ethylene glycol scattering. To best represent the temperature dependence of these modes, the absolute Raman cross sections of the 682, 731, and 892 cm^{-1} modes are plotted as a function of temperature in Figure 6A. This plot was generated by converting peak areas into Raman cross sections using eq 2. The Raman cross sections vs temperature for the 569, 682, 731, and 892 cm^{-1} modes fit roughly an inverse quadratic in temperature. As shown in Figure 6B, the cross sections depend on temperature as $\sim 1/T^{\alpha}$ where α ranges from ~1.3 to 1.8.

Excitation Profiles. Measurements of the Raman excitation profiles (REP) of the mid-frequency modes on a single RC sample are presented in Figure 7. The lack of spectral differences as excitation is tuned through the 800 nm band suggests that the two B molecules have the same multimode Franck−Condon factors. The peak heights for the 569, 682, 731, and 892 cm^{-1} RC modes and for the ethylene glycol standard derived from the data set shown in Figure 7 are plotted in Figure 8A along with the RC absorption spectrum for reference. The constant ethylene glycol scattering and the 0−0 enhancement in the RC modes are evident. Figure 8B presents the absolute Raman cross sections as a function of excitation wavelength calculated from one data set at 770 nm, four data sets at 780 nm, two data sets at 790, six data sets at 800 nm, one data set at 810 nm, and four data sets at 820 nm. The REPs show that these modes gain enhancement by coupling to the Q_y transitions. The start of enhancement due to the 0−1 vibronic band is also apparent for all the modes with 780 nm excitation (Figure 8B). The profiles in Figure 8A,B are somewhat different because the data shown in Figure 8A are derived from a single data set at each excitation wavelength, while the profiles shown in Figure 8B are generated from averages of multiple data sets.

Theoretical Modeling. Modeling the B Raman intensities, absorption spectra, and their temperature dependence reveals the vibronic dephasing time and nuclear distortions in the excited state of B. The self-consistent fitting routine consisted of the following steps: (1) We first adjust the relative displacements of the modes to find a model which fits not only the room-temperature absorption spectrum, but the 278 K relative Raman cross sections with 800 nm excitation. This can be done for a range of values of S_{tot}, homogeneous and inhomogeneous broadening. (2) Next, these models are restricted to those that

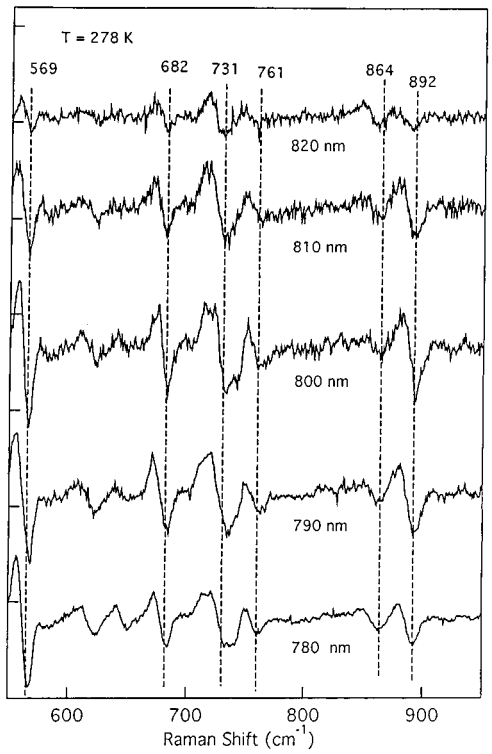

Figure 7. Mid-frequency SERDS spectra of B obtained at 278 K using 780, 790, 800, 810, and 820 nm excitation on the same sample in a 50% v/v mixture of buffer and ethylene glycol (OD at 800 nm = 0.51, power = 5−8 mW). All spectra were normalized to the intensity of the 864 cm^{-1} ethylene glycol mode.

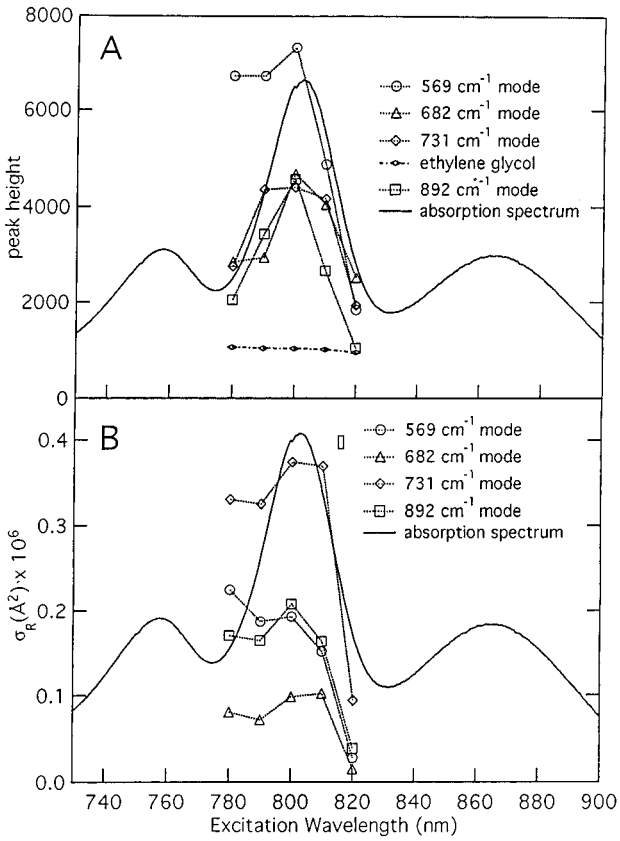

Figure 8. (A) Excitation profiles for the 569, 682, 731, and 892 cm^{-1} modes generated from the spectra in Figure 7. Peak heights for this single experiment are plotted against the excitation wavelength. The ethylene glycol intensity is constant. (B) Absolute Raman excitation profiles for the 569, 682, 731, and 892 cm^{-1} modes calculated from 1−6 data sets for each excitation wavelength. Experimental uncertainty ranges from 10−30%.

fit the *absolute* Raman cross sections with excitation at 800 nm at 278 K. The absorption and absolute REPs at 278 K can both be fit only for very few combinations of total *S* and homogeneous line-width values. (3) With the *S* values, transition moment length and the inhomogeneous broadening now fixed, the calculation is run at 95 K. The transition energy and homogeneous broadening are adjusted to fit the 77 K absorption spectrum. (4) Finally, the homogeneous line width is adjusted to reproduce the 731 cm^{-1} mode absolute Raman cross section at 95 K. No attempt was made to fit the relative Raman intensities at 95 K, although they agree fairly well with experiment for the modes >300 cm^{-1}. Below 300 cm^{-1} the calculated relative intensities are significantly above the experimental values.

Initially, a model was formulated assuming degenerate noninteracting transitions for the two B molecules. The identical absorption and REPs generated for each transition were then added and compared to the experimental data. The results of the best fit to the absorption spectra at 278 and 95 K for this model are shown in Figure 9A,B, respectively. The 17-mode model parameters and calculated resonance Raman intensities are presented in Table 2. For these calculations, the total *S* was 0.32 and the effective homogeneous decay time at 278 K was $T_2 = 54$ fs. This includes 54 cm^{-1} (fwhm) of Lorentzian broadening, corresponding to the measured energy-transfer time of ∼116 fs, and 283 cm^{-1} (fwhm) of Gaussian broadening. The effective dephasing time becomes ∼210 fs at 95 K. This includes 38 cm^{-1} of Lorentzian broadening, corresponding to the measured energy-transfer time of 163 fs at 85 K and 50 cm^{-1} of Gaussian broadening. The inhomogeneous spectral width of 247 cm^{-1} was defined by the fitting process at 278 K and kept constant for the 95 K fit. The calculated absolute Raman cross section for the 731 cm^{-1} mode with 800 nm excitation is 3.3×10^{-7} $Å^2$ at 278 K and 15.4×10^{-7} $Å^2$ at 95 K. These results are in good agreement with the experimental values of $\sim 3.7 \times 10^{-7}$ $Å^2$ and $\sim 14 \times 10^{-7}$ at 278 and 95 K, respectively.

We then explored a model employing two nondegenerate uncoupled transitions without changing the *S* values or homogeneous line widths (Figures 9C,D) with the goal of getting a better fit to the low-temperature absorption spectrum. At 278 K, both bands had a homogeneous line width of 278 cm^{-1} and an inhomogeneous line width of 123 cm^{-1}. At 95 K, both bands had a 109 cm^{-1} homogeneous line width, while the low-energy band had an inhomogeneous width of 212 cm^{-1} and the high-energy band had a 118 cm^{-1} inhomogeneous line width. The sums of the 800 nm absolute Raman cross sections for the 731 cm^{-1} mode from both transitions were calculated to be 3.1×10^{-7} $Å^2$ at 278 K and 16.1×10^{-7} $Å^2$ at 95 K, in good agreement with the measured values. The calculated REPs for the 569, 621 + 682, 731, and 892 cm^{-1} modes are shown in conjunction with the measured excitation profiles in Figure 10. The REPs generated for the nondegenerate states model differs very little from the REPs generated with the degenerate transition model.

Several other degenerate transition models were developed to explore the sensitivity of the parameters. For a model with a total *S* of 0.43, the entire spectral broadening had to be made homogeneous to fit the room-temperature spectra; to also achieve a fit to the 95 K absolute Raman cross sections, an inhomogeneous line width of 120 cm^{-1} had to be introduced and the homogeneous line width reduced to 30 cm^{-1}. This model was rejected because it is not physically realistic that the inhomogeneous broadening would increase as temperature is reduced, and with such a large total *S*, the 0−1 sideband was

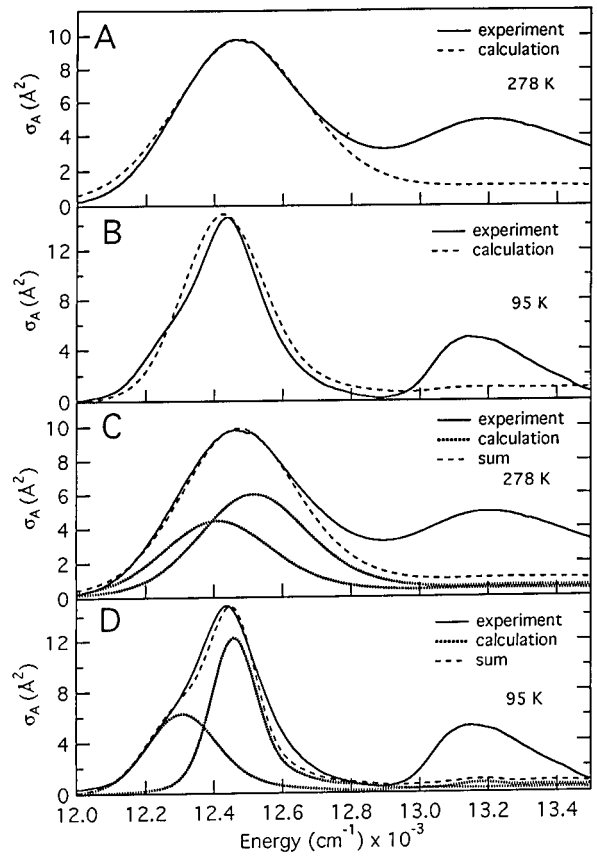

Figure 9. Absorption spectra of B at 278 K **(A)** and 95 K **(B)** calculated using the sum of two degenerate transitions. The calculated spectra (- - -) fit closely the experimental absorption spectra, except for the line shape of the 95 K spectrum. Parameters for these calculations are listed in Table 2. Absorption spectra of B at 278 K (C) and 95 K (D) calculated using two nondegenerate transitions. The individual spectra corresponding to each transition (···) and their sum (- - -) provide a better fit to the 95 K absorption spectrum.

more prominent than permitted by the experimental absorption spectrum. A total *S* much smaller than 0.25 is not able to reproduce both the absorption spectrum and the absolute Raman cross sections at 95 K. To investigate the small *S* limit, a model with a total *S* of 0.17, a Gaussian spectral width of 180 cm^{-1}, and an inhomogeneous distribution of 350 cm^{-1} fits the relative Raman cross sections, the absorption spectrum and the 278 K 731 cm^{-1} Raman cross section with 800 nm excitation. However, this model was not able to reproduce both the absorption spectrum and the absolute Raman cross sections at 95 K. Even with a homogeneous line width of only 5 cm^{-1},[49,50] the Raman cross section of the 731 cm^{-1} mode at 95 K was ~3 times too small. Through such studies, we believe that the total *S* must be between 0.3 and 0.35, and the effective dephasing time must be 50−60 fs at 278 K and 150−220 fs at 95 K. If the total *S* is much larger than 0.35, a strong 0−1 vibronic sideband develops[51,52] and the inhomogeneous parameter becomes nonphysical, while if it is much smaller than 0.30, it is impossible to reproduce the strong Raman cross sections observed at low temperature.

Preresonant Raman Intensities. The spectrum of B obtained with 800 nm excitation (Figure 3A) exhibits weak scattering in high-frequency vibrational modes. By comparison, spectra obtained of monomeric BChl and of RCs using the FT Raman technique with 1064 nm excitation generally have easily observable high-frequency modes.[19,53,54] On the basis of the vibronic model developed here we can understand this observation. The calculated values for the Raman cross sections of each mode of B with excitation at 1064 nm are presented in Figure 11. A substantial *relative* deenhancement of the lower frequency vibrations is observed with pre-resonant excitation. In fact, it is easy to see that vibrations with frequencies higher than 1600 cm^{-1} might not be observable at all in the spectrum excited on resonance but could appear with modest intensity in the preresonance spectrum. As expected, the *absolute* scattering strength is smaller by many orders of magnitude in the preresonance case. Thus, the differences between our resonance Raman spectra and the FT Raman results[19,53] are not anomalous and can be qualitatively reproduced with a single vibronic model.

Discussion

We are interested in studying the excited-state processes in B in order to gain insight into the fast dynamics and mechanism of energy and electron transfer in the RC. The proximity of B to P, along with its ability upon electronic excitation to transfer energy to P, make knowledge of its excited-state electronic and nuclear dynamics crucial to understanding electron transfer in the RC. This information is particularly pertinent to the exploration of the possible role of coherent nuclear dynamics in energy[55] and electron transfer[56,57] and in photochemistry.[58,59]

Pursuant to this goal, self-consistent modeling of resonance Raman excitation profiles in conjunction with electronic absorption spectra has been used to reveal the time scale on which electronic coherence is lost as well as the extent of nuclear distortion accompanying electronic excitation. The temperature dependence of the Raman cross sections and absorption spectrum provide more information about the mechanisms by which excited-state dephasing is induced and helps to constrain the total electron−nuclear coupling constants. A "best fit" set of parameters which summarizes the experimental results has been generated (Table 1) and can be used to help understand the excited-state dynamics of B.

Electronic Structure of the 800 nm Absorption Band. It has been proposed that the electronic structure of the RC is best characterized by a general "RC polarizability", in which the Q_y electronic states of the P, B, and H chromophores are mixed. Excitonic mixing of molecular states is a function of the interaction energy between them and results in delocalized states. Several calculations of the RC absorption spectrum suggest strong exciton interactions between the chromophores.[60,61] The opposite view considers the P, B_A, B_B, H_A, and H_B chromophores as independent. Experimental evidence for this description of the RC includes the Stark effect spectrum of the RC, which is best explained assuming independent transitions for each of the five chromophores (assuming a single exciton band for the P molecule).[62] These different pictures must be reconciled in order to understand the electronic structure of the 800 nm band and the mechanism of energy transfer.

Our Raman spectral data support the idea that the two states necessary to model the 800 nm band are not mixed states including P or H contributions.[63] Raman spectra excited throughout the B band have no bacteriopheophytin character, ruling out mixing between the B and H states in the 800 nm band (see also ref 64). The resonance Raman spectrum of P contains modes which are unique to the dimer but are not seen with excitation in the 800 nm band.[33] While our data cannot rule out a weak electronic contribution to the 800 nm band from the upper exciton band of P, neither do we see evidence that requires its presence.

We have used the same mode frequencies and electron−nuclear coupling constants for both the B_A and B_B transitions. Raman spectra acquired with excitation between 770 and 820 nm do not show significant variations in mode frequencies or

TABLE 2: 17-Mode Model of the Vibronic Properties of B at 278 and 95 K

ω, cm^{-1}	I(278 K)[a]	I(95 K)[a]	S[b]	I(278 K)[c]	σ_1(278 K)[d]	σ_2(278 K)[e]	I(sum)[f]	I(95 K)[g]	σ_1(95 K)[h]	σ_2(95 K)[i]	I(sum)[j]
84	0.55	0.55	0.027	0.49	0.55	1.04	0.51	2.47	4.16	36.53	2.52
117	0.35	0.47	0.013	0.33	0.39	0.68	0.35	1.19	2.74	15.14	1.11
177	1.43	1.12	0.036	1.34	1.63	2.59	1.36	2.77	10.10	28.70	2.41
212	1.30	0.56	0.028	1.18	1.47	2.20	1.18	1.90	8.35	19.26	1.71
332	0.63	0.40	0.013	0.61	0.76	1.07	0.59	0.59	2.48	7.33	0.61
355	0.49	0.73	0.010	0.46	0.57	0.81	0.45	0.43	1.61	5.53	0.44
384	0.59	0.89	0.013	0.58	0.72	1.03	0.56	0.53	1.69	7.05	0.54
464	0.20	0.53	0.005	0.20	0.25	0.37	0.20	0.19	0.41	2.59	0.19
569	0.41	0.55	0.011	0.40	0.47	0.76	0.40	0.38	0.68	5.46	0.38
682	0.47	0.59	0.014	0.47	0.53	0.91	0.46	0.46	0.75	6.67	0.46
731	1.00	1.00	0.031	1.00	1.13	1.97	1.00	1.00	1.58	14.54	1.00
761	0.18	0.19	0.006	0.19	0.22	0.38	0.19	0.19	0.30	2.79	0.19
892	0.80	0.99	0.027	0.80	0.89	1.62	0.81	0.82	1.23	12.04	0.82
1002	0.55	1.04	0.020	0.57	0.63	1.16	0.58	0.59	0.86	8.63	0.59
1114	0.41	0.49	0.014	0.38	0.42	0.79	0.39	0.40	0.57	5.85	0.40
1165	0.90	0.91	0.033	0.89	0.96	1.83	0.90	0.92	1.31	13.57	0.92
1535	0.40	0.39	0.017	0.41	0.43	0.85	0.41	0.43	0.58	6.29	0.43

[a] Measured Raman intensities at $\lambda_{ex} = 800$ nm are relative to the sum of the intensities of the 726 + 736 + 747 cm^{-1} modes at 95 K and the 721 + 731 + 744 cm^{-1} modes at 278 K. [b] Linear electron−nuclear coupling constants. The same set of S values was used for all calculations presented here. [c] Calculated relative Raman intensities for the degenerate transitions model at 278 K. For this model, transition moment (M) = 2.63, transition energy (E_{00}) = 802.57 nm, homogeneous line width (Γ_h) = 23 cm^{-1} (Lorentzian) and 85 cm^{-1} (Gaussian) and inhomogeneous line width (Γ_{inh}) = 105 cm^{-1}. [d] Calculated Raman cross sections ($\times 10^{-7}$ Å^2) at 278 K for the low-energy band of the nondegenerate transitions model. For this band, $M = 1.92$, $E_{00} = 806.45$ nm, $\Gamma_h = 23$ cm^{-1} (Lorentzian) and 85 cm^{-1} (Gaussian) and $\Gamma_{inh} = 55$ cm^{-1}. [e] Calculated Raman cross sections ($\times 10^{-7}$ Å^2) at 278 K for the high-energy band of the nondegenerate-transitions model. For this band, $M = 1.66$, $E_{00} = 799.68$ nm, Γ_h = 23 cm^{-1} (Lorentzian) and 85 cm^{-1} (Gaussian) and $\Gamma_{inh} = 55$ cm^{-1}. [f] Calculated relative Raman intensities for the summed intensities from the two-transition model at 278 K. [g] Calculated relative Raman intensities for the degenerate transitions model at 95 K. For this model, $M = 2.63$, E_{00} = 805.15 nm, $\Gamma_h = 16$ cm^{-1} (Lorentzian) and 15 cm^{-1} (Gaussian) and $\Gamma_{inh} = 105$ cm^{-1}. [h] Calculated Raman cross sections ($\times 10^{-7}$ Å^2) at 95 K for the low-energy band of the nondegenerate-transitions model. For this band, $M = 1.66$, $E_{00} = 812.81$ nm, $\Gamma_h = 16$ cm^{-1} (Lorentzian) and 15 cm^{-1} (Gaussian) and $\Gamma_{inh} = 90$ cm^{-1}. [i] Calculated Raman cross sections ($\times 10^{-7}$ Å^2) at 95 K for the high-energy band of the nondegenerate-transitions model. For this band, $M = 1.86$, $E_{00} = 802.27$ nm, $\Gamma_h = 16$ cm^{-1} (Lorentzian) and 15 cm^{-1} (Gaussian) and $\Gamma_{inh} = 55$ cm^{-1}. [j] Calculated relative Raman intensities for the summed intensities from the nondegenerate transitions model at 95 K.

TABLE 3: Temperature Dependence of the Dephasing Time of B

temp (K)	Lorentzian Γ_h (cm^{-1})	Gaussian Γ_h (cm^{-1})	effective T_2 (fs)
95 K	16[a]	15[c]	∼210[e]
278 K	23[b]	85[d]	∼54[e]

[a] Determined from the single exponential time constant, 163 ± 54 fs, from Stanley et al. measured at 85 K.[15] [b] Determined from the single exponential time constant, 116 ± 35 fs, at 298 K from Jia et al.[14] [c] Gaussian decay comprising the remainder of the broadening necessary to fit both the absorption and Raman from the calculation shown in Figure 9A. [d] Gaussian decay comprising the remainder of the broadening necessary to fit both the absorption and Raman from the calculation shown in Figure 9B. [e] Determined from the 1/e time of the function specified by the exponential multiplied by the Gaussian damping function.

relative intensities, supporting this assumption. This is also bolstered by our earlier Raman spectrum of B in the RC from *Cf. aurantiacus*, which contains only one B molecule (see ref 39 and references therein). The agreement between the *Rb. sphaeroides* B Raman spectrum and the *Cf. aurantiacus* B spectrum supports the idea that B_A and B_B have similar vibronic properties.

While the fits to the absorption spectra are qualitatively acceptable there are deficiencies in the fit to the 77 K absorption spectrum, even when two nondegenerate transitions are used. One possible explanation is that the two B molecules have somewhat different vibronic properties. Another possibility is that the shoulder on the low-energy side of the B band at 77 K is due to the upper exciton band of P. A number of measurements have suggested the presence of this weak band.[62,65−67]

No terms are included in our calculation to allow us to model non-Condon contributions to the Raman scattering. Several studies of porphyrins and pheophytins show that some modes have up to 40% contributions to their Q_y REPs from non-Condon scattering sources (see for example refs 68 and 69). It would be necessary to measure the 0−1 part of the REPs, which for many of the B modes lie in the same spectral region as the H absorption band, to determine whether non-Condon scattering may be occurring. Since Raman spectra acquired with excitation in the ∼770−700 nm range contain both B and H modes,[64] the detailed REPs for B necessary to distinguish modes which may gain enhancement from vibronic coupling mechanisms would be difficult to obtain. However, the REPs for most of the Raman bands observed here match the calculated REPs shown in Figure 10 and their depolarization ratios are in the ∼0.3−0.5 range.

In summary, whether the RC is best described with localized or with delocalized electronic transitions is the key to understanding the energy-transfer mechanism between the 800 and 870 nm bands. For a system of delocalized, highly coupled states, energy transfer is actually an internal conversion process. On the other hand, in the local states picture, direct orbital overlap has been proposed as the energy transfer mechanism most consistent with the measured fast rate (∼100 fs).[8,14,15] Our analysis of B is most consistent with a picture in which B_A and B_B have independent, nearly degenerate transitions, with similar vibronic characteristics.

Nuclear Dynamics. Resonance Raman scattering provides information on the frequencies of nuclear motion and their relative amplitudes on the 0−50 fs time scale. It is an excellent method for determining the initial nuclear dynamics, because its resolution is limited only by the vibronic dephasing time as opposed to the time resolution imposed by the instrumentation in time-resolved experiments. Only recently have studies begun to suggest a role for nuclear dynamics in the mechanisms of energy transfer,[55] electron transfer,[56,57] and photochemistry.[58,59] Measurements of the femtosecond stimulated[57] and spontaneous emission[56] from P in the RC exhibit strong low-frequency oscillations, corresponding to coherent nuclear motions which decay on the time scale of electron transfer. These oscillation

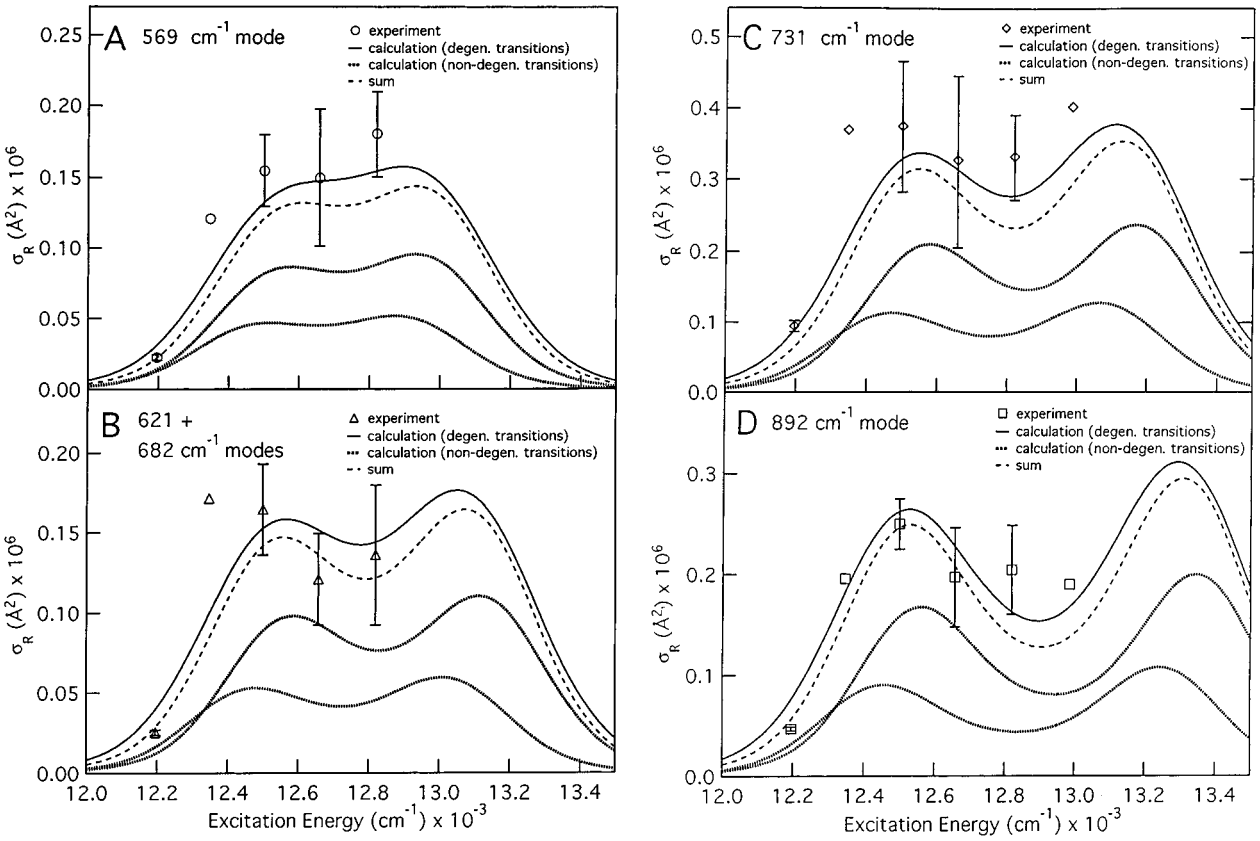

Figure 10. Comparison of the experimental Raman excitation profiles of the (A) 569, (B) 621 + 682, (C) 731, and (D) 892 cm^{-1} modes with the calculated REPs at 278 K using the degenerate transition model and the nondegenerate-transitions model.

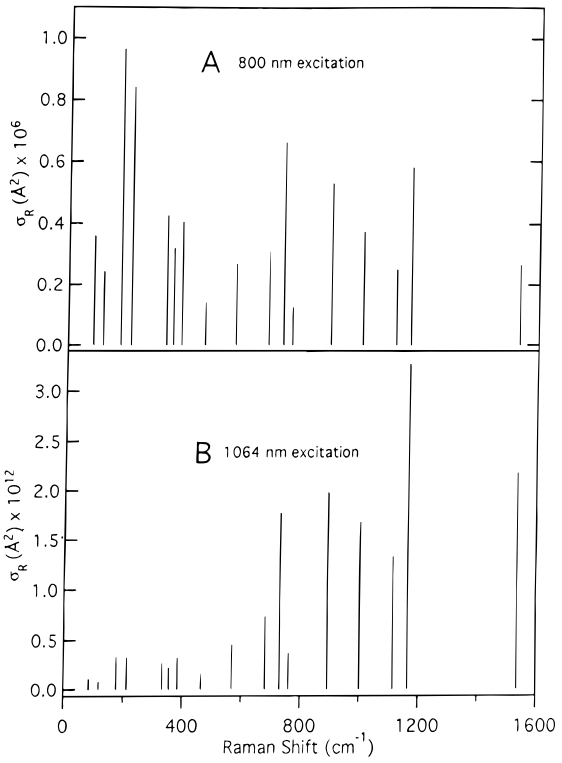

Figure 11. Calculated Raman intensities of B using the parameters shown in Table 2 (degenerate transitions model) as the excitation is tuned from (A) being directly on resonance (800 nm) to (B) being preresonant (1064 nm).

frequencies and their relative intensities match very well with the resonance Raman spectrum of P which we reported earlier.[33] This makes sense since the Franck−Condon coupled modes that generate intense Raman scattering should also exhibit significantly displaced excited-state potentials.[70] We have also shown that there is reasonable agreement between the resonance Raman spectrum and the coherent oscillation power spectrum derived from femtosecond-stimulated emission spectra of chlorosomes.[40,55] Our analysis of B provides the frequencies and mode-specific coupling constants that describe the nuclear motions which are initiated with 800 nm excitation. When it is possible to resolve the stimulated emission from B with high time resolution, oscillations corresponding to the Raman modes of B reported here should be observed. Assignment of these modes would provide the coordinates along which B distorts and reveal how they affect orbital overlap with and energy transfer to P.

Excited-State Dephasing in B. The time-dependent overlap of the stationary ground-state wave function with an evolving excited-state wave function determines the magnitude of the Raman cross sections. This overlap is damped in the excited-state by a dephasing time which thus controls the magnitude of the Raman cross sections. The dephasing time, or T_2, is defined in relation to the homogeneous line width for exponential decays as

$$\Gamma_h = \frac{h}{T_2} = \frac{h}{2T_1} + \frac{h}{T_2^*} \qquad (3)$$

where T_2^* is the pure dephasing time, and T_1 is the population relaxation time. In the modeling done here, the dephasing was partitioned into an exponential lifetime component corresponding to the measured energy transfer time (116 ± 35 fs[14] at 298 K and 163 ± 54 fs at 85 K[15]) and a Gaussian pure dephasing component. Thus, the effective dephasing time contains contributions from both pure dephasing and population relaxation and is determined by finding the 1/e time of the product of the exponential and the Gaussian decay functions.

The effective dephasing time found here is ∼54 fs at 278 K and ∼210 fs at 95 K. The modeling was performed with

both Lorentzian (corresponding to the energy transfer time) and Gaussian (corresponding to the pure dephasing component) broadening with the resulting effective dephasing times shown in Table 3. At 278 K the effective dephasing time (∼54 fs) is clearly limited by the pure dephasing component (283 cm^{-1} fwhm), while at 95 K the effective dephasing time (∼210 fs) is faster than the lifetime component ($2T_1 \sim 326$ fs) but not limited by the broadening introduced by the pure dephasing component (50 cm^{-1}). The systematically elevated calculated Raman intensities of modes below ∼300 cm^{-1} compared to the measured cross sections at 95 K suggests that the T_2 used in our calculation is not fast enough at this temperature. Thus, the damping function is slower than the observed intensities suggest. This is the only inconsistency in our model and may arise from an inadequate pure dephasing functional form. It may be possible to resolve this discrepancy with a damping function more accurately representing the pure dephasing processes.

While the population decay calculated in our model for B clearly should correspond to the energy transfer time from B* to P, the fact that the 278 K Raman intensities are unchanged upon chemical oxidation of P suggests that an alternative and equally fast relaxation pathway exists when P is oxidized. In agreement with this result, Jia et al. directly measured the population dynamics of B using ultrafast pump−probe techniques and found that the kinetic component corresponding to energy transfer from B did not change when P was oxidized.[14] The most obvious alternative T_1 relaxation pathway in the K_3-$Fe(CN)_6$-treated sample would be energy transfer to P^+.

The fast T_2* (∼54 fs) for B at room temperature is most likely due to coupling to low-frequency intramolecular, protein, and solvent modes. These are modes that are unobservable in the Raman spectrum either because they are very low in frequency or because of a broad vibrational line width or distribution. In general, solute−solvent coupling leads to Lorentzian and Gaussian homogeneous bandwidths in the limits of weak and strong coupling.[71] The solute−solvent coupling has also been described in terms of the time scale on which it occurs as the fast and slow modulation limits, corresponding respectively to Lorentzian and Gaussian line shapes.[50,72] Our finding that the B absorption band is best modeled with a Gaussian homogeneous line width indicates that there is strong coupling to the bath (slow modulation limit). In this limit, the time scale for site-interconversion processes for a spectral distribution (of width Γ) of E_{00}'s are slower than h/Γ, but they contribute to the homogeneous line width for Raman scattering because they are faster than the vibrational dephasing time**.** Since the Raman cross sections depend on the homogeneous line width as $1/\Gamma_h^2$ for a Gaussian line width, if the dephasing time decreases linearly with temperature, the dependence of the Raman cross section on temperature would scale as $1/T^2$. In fact we observe an approximate inverse quadratic dependence of the Raman cross sections on temperature. Thus, as the temperature is decreased below some limiting temperature, the Raman cross sections should cease to gain intensity as they would be damped only through population decay corresponding to energy transfer.

There have been very few explicit studies of the dependence of absolute Raman cross sections on temperature. In one such study, Schomacker et al. found the cross sections for ferrocytochrome *c* to be nearly temperature independent.[32] However, ferrocytochrome *c* is a clear case where pure dephasing is of little if any importance, since its T_1 is ∼14 fs. In the case of B, where T_1 is in the 116−140 fs range,[8,14,15] coupling to low-frequency intramolecular, protein and solvent modes becomes quite important in determining the overall homogeneous line width.

Preresonant Relative Raman Intensities. The relative Raman intensities calculated for 800 and 1064 nm excitation differ because as excitation is tuned from 800 to 1064 nm, the scattering shifts from the "long-time" to the "short-time" scattering limit.[26] In the "long-time" limit, the Raman cross sections scale as *S*. This limit is observed whenever the effective dephasing time is long in comparison to the period of the Raman mode in question. The "short-time" limit is observed when the effective dephasing time is fast compared to the vibrational period. Off-resonant intensities (such as those calculated in Figure 11B) scatter in the "short-time" limit because the time is set by the large detuning energy. The intensities of the modes in the resonance Raman spectrum of B having frequencies below 300 cm^{-1} thus scale as $\sim S\omega^2$. The "short-time" limit arises in the resonance Raman spectrum for modes which are of low enough frequency that they are not able to build up substantial overlap between the ground and excited-state before the excited-state dephases. This provides a clear physical picture for the observed deenhancement of the low-frequency modes in the FT Raman spectra.

Conclusions. The initial excited-state nuclear and electronic dynamics of B and the temperature dependence of the electronic dynamics have been characterized through measurement and modeling of resonance Raman intensities. Our data are most consistent with a model in which the 800 nm band arises from independent nearly degenerate Q_y transitions of the two B molecules. The temperature dependent excited-state dephasing time of B reveals that while energy transfer is an important contributor to the loss of coherence in the excited state of B, intramolecular multimode processes along with significant coupling to the bath dominate the homogeneous line width at room temperature and continue to contribute even at 95 K. This work provides a more detailed picture of the electronic and nuclear dynamics of B. A similar study is presently being completed on the photophysics of P, and will be published separately.

Acknowledgments. This work was funded by Grant CHE 94−19714 from the National Science Foundation to RAM. A.P.S. was supported by a National Institutes of Health Postdoctoral Fellowship (GM 14298). S.G.B. thanks the National Science Foundation Biophysics Program for its support.

References and Notes

(1) Abbreviations: reaction center, RC; bacteriochlorophyll, BChl; accessory bacteriochlorophylls, B; special pair, P; Raman excitation profile, REP; Fourier transform, FT.

(2) Kirmaier, C.; Holten, D. *Photosynth. Res.* **1987**, *13*, 225.

(3) Feher, G. *Annu. Rev. Biochem.* **1989**, *58*, 607.

(4) Friesner, R. A.; Won, Y. *Biochim. Biophys. Acta* **1989**, *977*, 99.

(5) Boxer, S. G.; Goldstein, R. A.; Lockhart, D. J.; Middendorf, T. R.; Takiff, L. *J. Phys. Chem.* **1989**, *93*, 8280.

(6) Fleming, G. R.; van Grondelle, R. *Phys. Today* **1994**, *47*, 48.

(7) Woodbury, N. W.; Becker, M.; Middendorf, D.; Parson, W. W. *Biochemistry* **1985**, *24*, 7516.

(8) Martin, J.-L.; Breton, J.; Hoff, A. J.; Migus, A.; Antonetti, A. *Proc. Natl. Acad. Sci. U.S.A.* **1986**, *83*, 957.

(9) Kirmaier, C.; Holten, D. *Proc. Natl. Acad. Sci. U.S.A.* **1990**, *87*, 3552.

(10) Du, M.; Rosenthal, S. J.; Xie, X.; DiMagno, T. J.; Schmidt, M.; Hanson, D. K.; Schiffer, M.; Norris, J. R.; Fleming, G. R. *Proc. Natl. Acad. Sci. U.S.A.* **1992**, *89*, 8517.

(11) Müller, M. G.; Griebenow, K.; Holzwarth, A. R. *Chem. Phys. Lett.* **1992**, *199*, 465.

(12) Hamm, P.; Gray, K. A.; Oesterhelt, D.; Feick, R.; Scheer, H.; Zinth, W. *Biochim. Biophys. Acta* **1993**, *1142*, 99.

(13) Vos, M. H.; Lambry, J.-C.; Robles, S. J.; Youvan, D. C.; Breton, J.; Martin, J.-L. *Proc. Natl. Acad. Sci. U.S.A.* **1991**, *88*, 8885.

(14) Jia, Y.; Jonas, D. M.; Joo, T. H.; Nagasawa, Y.; Lang, M. J.; Fleming, G. R. *J. Phys. Chem.* **1995**, *99*, 6263.
(15) Stanley, R. J.; King, B.; Boxer, S. G. *J. Phys. Chem.* **1996**, *100*, 12052.
(16) Kirmaier, C.; Holten, D. *Biochemistry* **1991**, *30*, 609.
(17) Arlt, T.; Schmidt, T. S.; Kaiser, W.; Lauterwasser, C.; Meyer, M.; Scheer, H.; Zinth, W. *Proc. Natl. Acad. Sci. U.S.A.* **1993**, *90*, 11757.
(18) Small, G. J. *Chem. Phys.* **1995**, *197*, 239.
(19) Mattioli, T. A.; Hoffmann, A.; Sockalingum, D. G.; Schrader, B.; Robert, B.; Lutz, M. *Spectrochim. Acta* **1993**, *49A*, 785.
(20) Diers, J. R.; Bocian, D. F. *J. Am. Chem. Soc.* **1995**, *117*, 6629.
(21) Lao, K.; Moore, L. J.; Zhou, H. L.; Boxer, S. G. *J. Phys. Chem.* **1995**, *99*, 496.
(22) Middendorf, T. R.; Mazzola, L. T.; Lao, K. Q.; Steffen, M. A.; Boxer, S. G. *Biochim. Biophys. Acta* **1993**, *1143*, 223.
(23) Lösche, M.; Feher, G.; Okamura, M. Y. *Proc. Natl. Acad. Sci. U.S.A.* **1987**, *84*, 7537.
(24) Gillie, J. K.; Small, G. J.; Golbeck, J. H. *J. Phys. Chem.* **1989**, *93*, 1620.
(25) Reddy, N. R. S.; Small, G. J.; Seibert, M.; Picorel, R. *Chem. Phys. Lett.* **1991**, *181*, 391.
(26) Myers, A. B.; Mathies, R. A. In *Biological Applications of Raman Spectrometry: Vol. 2—Resonance Raman Spectra of Polyenes and Aromatics*, Spiro, T. G., Ed.; John Wiley: New York, 1987; p 1.
(27) Sue, J.; Mukamel, S. *J. Chem. Phys.* **1988**, *88*, 651.
(28) Loppnow, G. R.; Mathies, R. A. *Biophys. J.* **1988**, *54*, 35.
(29) Phillips, D. L.; Myers, A. B. *J. Chem. Phys.* **1991**, *95*, 226.
(30) Morikis, D.; Li, P.; Bangcharoenpaurpong, O.; Sage, J. T.; Champion, P. T. *J. Phys. Chem.* **1991**, *95*, 3391.
(31) Myers, A. B.; Harris, R. A.; Mathies, R. A. *J. Chem. Phys.* **1983**, *79*, 603.
(32) Schomacker, K. T.; Champion, P. M. *J. Chem. Phys.* **1989**, *90*, 5982.
(33) Cherepy, N. J.; Shreve, A. P.; Moore, L. J.; Boxer, S. G.; Mathies, R. A. *J. Phys. Chem.* **1994**, *98*, 6023.
(34) Schenck, C. C.; Blankenship, R. E.; Parson, W. W. *Biochim. Biophys. Acta* **1982**, *680*, 44.
(35) Okamura, M.; Isaacson, R. A.; Feher, G. *Proc. Nat. Acad. Sci. U.S.A.* **1975**, *72*, 3491.
(36) Shreve, A. P.; Cherepy, N. J.; Franzen, S.; Boxer, S. G.; Mathies, R. A. *Proc. Natl. Acad. Sci. U.S.A.* **1991**, *88*, 11207.
(37) Mathies, R.; Yu, N.-T. *J. Raman Spectrosc.* **1978**, *7*, 349.
(38) Shreve, A. P.; Cherepy, N. J.; Mathies, R. A. *Appl. Spectrosc.* **1992**, *46*, 707.
(39) Cherepy, N. J.; Holzwarth, A. R.; Mathies, R. A. *Biochemistry* **1995**, *34*, 5288.
(40) Cherepy, N. J.; Du, M.; Holzwarth, A. R.; Mathies, R. A. *J. Phys. Chem.* **1996**, *100*, 4662.
(41) Lawless, M. K.; Mathies, R. A. *J. Chem. Phys.* **1992**, *96*, 8037.
(42) Albrecht, A. C.; Hutley, M. C. *J. Chem. Phys* **1971**, *55*, 4438.
(43) Trulson, M. O.; Mathies, R. A. *J. Chem. Phys.* **1986**, *84*, 2068.
(44) To fit only three data points using eq 1, it was found necessary to estimate the value of ω_e, which was then held fixed. The details of this fitting procedure are not critical, since the actual best fit differs only marginally from a simple ω^4 extrapolation of the visible cross section data.
(45) Straley, S. C.; Parson, W. W.; Mauzerall, D. C.; Clayton, R. K. *Biochim. Biophys. Acta* **1973**, *305*, 597.
(46) Shreve, A. P.; Mathies, R. A. *J. Phys. Chem.* **1995**, 7285.
(47) The models were calculated at 278 and 95 K because the measurements of the absolute scattering cross section of the 730 cm^{-1} mode and the full spectra were made at these temperatures. However, the model was fit to our highest quality absorption spectra which were acquired at 298 and 77 K. The absorption spectra vary insignificantly between 278 and 298 K and between 77 and 95 K.
(48) Cherepy, N. J.; Shreve, A. P.; Moore, L. J.; Boxer, S. G.; Mathies, R. A., in preparation.
(49) Such a small homogeneous linewidth would remove the model from the rapid fluctuation limit where electronic dephasing is fast relative to vibrational dephasing, calling into question the Kramers−Heisenberg treatment of the resonance emission.
(50) Mukamel, S. *Rev. Adv. Chem. Phys.* **1987**, *70*, 165.
(51) The 0−1 vibronic sideband of B is mostly hidden underneath the H absorption band. However, the absorption spectrum of RCs from which both bacteriopheophytins have been removed and replaced by blue-shifted pheophytins shows only a weak 0−1 sideband (<10% of the 0−0 band) for B.
(52) Scheer, H.; Meyer, M.; Katheder, I. In *The Photosynthetic Bacterial Reaction Center II*; Breton, J., Verméglio, A., Eds.; Plenum Press: New York, 1992; p 49.
(53) Johnson, C. K.; Rubinovitz, R. *Spectrochim. Acta* **1991**, *47A*, 1413.
(54) Noguchi, T.; Furukawa, Y.; Tasumi, M. *Spectrochim. Acta* **1991**, *47A*, 1413.
(55) Savikhin, S.; van Noort, P. I.; Blankenship, R. E.; Struve, W. S. *Biophys. J.* **1995**, *69*, 1100.
(56) Stanley, R. J.; Boxer, S. G. *J. Phys. Chem.* **1995**, *99*, 859.
(57) Vos, M. H.; Jones, M. R.; Breton, J.; Lambry, J.-C.; Martin, J.-L. *Biochemistry* **1996**, *35*, 2687.
(58) Wang, Q.; Schoenlein, R. W.; Peteanu, L.; Mathies, R. A.; Shank, C. V. *Science* **1994**, *266*, 422.
(59) Zhu, L.; Sage, J. T.; Champion, P. M. *Science* **1994**, *266*, 629.
(60) Thompson, M. A.; Zerner, M. C. *J. Am. Chem. Soc.* **1991**, *113*, 8210.
(61) Parson, W. W.; Warshel, A. *J. Am. Chem. Soc.* **1987**, *109*, 6152.
(62) Steffen, M. A.; Lao, K. Q.; Boxer, S. G. *Science* **1994**, *264*, 810.
(63) If the transitions underlying the 800 nm band do not arise from mixed states, it is not necessary to consider possible Raman interference effects due to the close-lying transitions.
(64) Cherepy, N. J.; Shreve, A. P.; Moore, L. J.; Boxer, S. G.; Mathies, R. A. *Biochemistry*, in press.
(65) Breton, J. *Biochim. Biophys. Acta* **1985**, *810*, 235.
(66) Verméglio, A.; Breton, J.; Paillotin, G.; Cogdell, R. J. *Biochim. Biophys. Acta* **1978**, *501*, 514.
(67) Rosenbach-Belkin, V.; Fisher, J. R. E.; Scherz, A. *J. Am. Chem. Soc.* **1991**, *113*, 676.
(68) Shelnutt, J. A.; Cheung, L. D.; Chang, R. C. C.; Yu, N.-T.; Felton, R. H. *J. Chem. Phys.* **1977**, *66*, 3387.
(69) Mattioli, T. A.; Haley, L. V.; Koningstein, J. A. *Chem. Phys.* **1990**, *140*, 317.
(70) Pollard, W. T.; Mathies, R. A. *Annu. Rev. Phys. Chem.* **1992**, *43*, 497.
(71) Zakaraya, M. G.; Ulstrup, J. *Chem. Phys.* **1989**, *135*, 49.
(72) Myers, A. B. *J. Opt. Soc. Am. B* **1990**, *7*, 1665.